Supplementary materials

Hierarchical Co-FeS_2/CoS_2 Heterostructures as a Superior Bifunctional Electrocatalyst

Ka Wang, Weilan Guo, Shancheng Yan, Haizeng Song, Yi Shi

In this work, we gradually optimized the experimental conditions before obtaining Co-FeS_2/CoS_2 heterostructures with superior electrocatalytic properties. The optimization of the experimental procedures includes the following five parts: selection of sulfur source, regulation of cobalt content, optimization of the load, using thiourea and sulfur powder as sulfur sources, and improving the dual sulfur source. All above reactions were maintained at 180℃for 8 hours. The figures show the overpotentials of OER at a current density of 10 mA cm^{-2} and the overpotentials of HER at a current density of -10 mA cm^{-2}.

Firstly, in the experiment, $FeSO_4 \cdot 7H_2O$ was prepared in 1 mM concentration and each sulfur source was set as 2.2 mM. As shown in Fig. S1, XRD patterns shows that the synthesized products using $Na_2S \cdot 9H_2O$, $SC(NH_2)_2$, CH_3CSNH_2, sulfur powder(S) as sulfur sources are FeS_2. Fig.S2 shows four FeS_2 with different nanostructures, it can also be seen that the low loading of the four FeS_2 on carbon cloths and the combination of products with carbon fibers are not very tight. Fig. S3 shows that the HER and OER performance of FeS_2 are not superior, but FeS_2 (S) and $FeS_2(SC(NH_2)_2)$ have better performance. From this weselected sulfur powder (S) and $SC(NH_2)_2$ as sulfur sources for the subsequent experiments.

Secondly, based on the results of the first experiment, we improved the electrocatalytic performances of $FeS_2(SC(NH_2)_2)$ and FeS_2 (S) by cobalt doping. As shown in Fig. S4, the electrocatalytic performances of $FeS_2(SC(NH_2)_2)$ and FeS_2(S) were changed by the incorporation of different proportions of cobalt. We found that when $FeS_2(SC(NH_2)_2)$ was doped with 13% (Co:Fe atom ratio) cobalt and FeS_2(S) was doped with 16.7% (Co:Fe atom ratio) cobalt, the electrocatalytic performances were better. Fig. S5 shows the XRD patterns and the Raman patterns for Co-$FeS_2(SC(NH_2)_2)$ and Co-FeS_2(S). From the XRD patterns, their crystal structures are not very dissimilar compared with $FeS_2(SC(NH_2)_2)$ and FeS_2(S). However, the Raman peak of Co-$FeS_2(SC(NH_2)_2)$ and Co-FeS_2(S) red-shifted as compared with $FeS_2(SC(NH_2)_2)$ and FeS_2(S). Fig. S6 shows the SEM images of Co-$FeS_2(SC(NH_2)_2)$ and Co-FeS_2(S). It can be seen that the doping of cobalt increases the product loading.

Thirdly, we also changed the molar of reactants to adjust the load on the carbon cloth. Fig. S7 shows that Co-FeS_2 has the best electrocatalytic performance when the molar ratio was 1.2 compared with the previous step, hence determining the amount of reactants used in subsequent experiments.

Fourthly, based on the results of the above three experiments, we continued to improve the experimental conditions. The $FeSO_4 \cdot 7\ H_2O$ (1.2 mM), $Co(NO_3)_2 \cdot 6\ H_2O$ (0.156 mM), and thiourea (1.8 mM) concentrations were determined. We added sulfur powder as sulfur sources at the same time, and the sulfur powder was gradually increased. Fig. S8a, b show that when 1.8 mM thiourea and 0.72 mM sulfur powder were used as the sulfur source, the electrocatalytic performance of Co-FeS_2 was

optimized. As shown in Fig. S8c-h, SEM images show two Co-FeS_2 synthesized using 1.8 mM thiourea and 0.72 mM or 0.96 mM sulfur powder, we found no significant difference in the morphology of these two Co-FeS_2.

Finally, because sulfur powder is insoluble in water, resulting in the low utilization rate of sulfur powder, we further optimized the procedure. $FeSO_4 \cdot 7H_2O$, $Co(NO_3) \cdot 6H_2O$, $SC(NH_2)_2$ were stirred in the reaction kettle for 15 minutes to form a uniform solution, and the weighed sulfur powder was added into the reaction kettle to continue stirring for 15 minutes. The magnetic stirrer was then removed. A thin layer of sulfur powder can be observed to form on the surface of the solution. Finally, the clean and dry carbon cloth was slowly placed into the reaction kettle along the middle location of the liquid surface, so that the sulfur powder is evenly attached to both sides of the carbon cloth, the reaction kettle was maintained at 180℃ for 8 hours. After the reaction was cooled to room temperature, cleaned, dried and tested. Fig. S9a shows the excellent electrocatalytic performance of the two Co-FeS_2/CoS_2 heterostructures, Co-FeS_2/CoS_2($SC(NH_2)_2$+0.72 S) and Co-FeS_2/CoS_2($SC(NH_2)_2$+ 0.96 S) were capable of drive a current density -10 mA cm^{-2} at overpotential of -103 mV and -110 mV. Fig. S9b shows that the Tafel slope of Co-FeS_2/CoS_2 were 56 mV dec^{-1} and 63 mV dec^{-1}. As shown in Fig. S9c, d, the morphology of Co-FeS_2/CoS_2($SC(NH_2)_2$+0.72 S) was the same as in Fig.1. Fig. S9e,f show microflower-like morphology of Co-FeS_2/CoS_2($SC(NH_2)_2$+0.96 S).

The electrochemical active surface area (ECSA) is a critical factor to affect the capability of water splitting electrocatalysts, since C_{dl} is linearly proportional to the

ECSA. To understand the origin of the superior activity of the Co-FeS_2/CoS_2 heterostructures electrocatalyst, the electrochemical double layercapacitance (C_{dl}) was estimated via simple CV tests. As shown in Fig. S10 a-c, current densities were recorded in a non-Faradic potential window with different scan rates (2, 5, 10, 20, 40, 80, and 160 mV s^{-1}), cyclic voltammograms of Co-FeS_2/CoS_2, Co-FeS_2(S), and Co-FeS_2 ($SC(NH_2)_2$) were measured in the non-faradaic capacitance current range. As shown in Fig. S10d, the C_{dl} value of hierarchical Co-FeS_2/CoS_2 is 86 mF cm^{-2} is larger than that of Co-FeS_2(S) (37 mF cm^{-2}) and 4.3 times of that of Co-FeS_2($SC(NH_2)_2$) (20 mF cm^{-2}). Intuitively, the hierarchical Co-FeS_2/CoS_2 heterostructures own more enhanced ECSA than the Co-FeS_2(S) and the Co-FeS_2($SC(NH_2)_2$). The result indicates that hierarchical architecture and bump feature can maximize the exposure of accessible active sites, which contributes to excellent electrocatalytic performance of Co-FeS_2/CoS_2 heterostructures. Furthermore, as shown in Fig. S10 e, the reaction kinetics is verified by EIS, the hierarchical Co-FeS_2/CoS_2 heterostructures present a smaller semicircle than Co-FeS_2(S) and Co-FeS_2($SC(NH_2)_2$) , which can be associated with interfacial charge transfer process, a lower value corresponds to a faster electron transfer rate. This result demonstrated further the faster catalytic kinetics of Co-FeS_2/CoS_2 heterostructures.

In the practical applications, stability remains an extremely important evaluation method for the performance of electrocatalysts. In addition to catalytic activity, we also analyzed the characterization results of the Co-FeS_2/CoS_2 heterostructures before and after the 1000 cycles. As shown in Fig. S11, it was found that the XRD patterns,

XPS spectra, SEM, and TEM images of Co-FeS_2/CoS_2 heterostructures did not significantly changed, which also indicated that the Co-FeS_2/CoS_2 heterostructures had superior electrochemical stability.

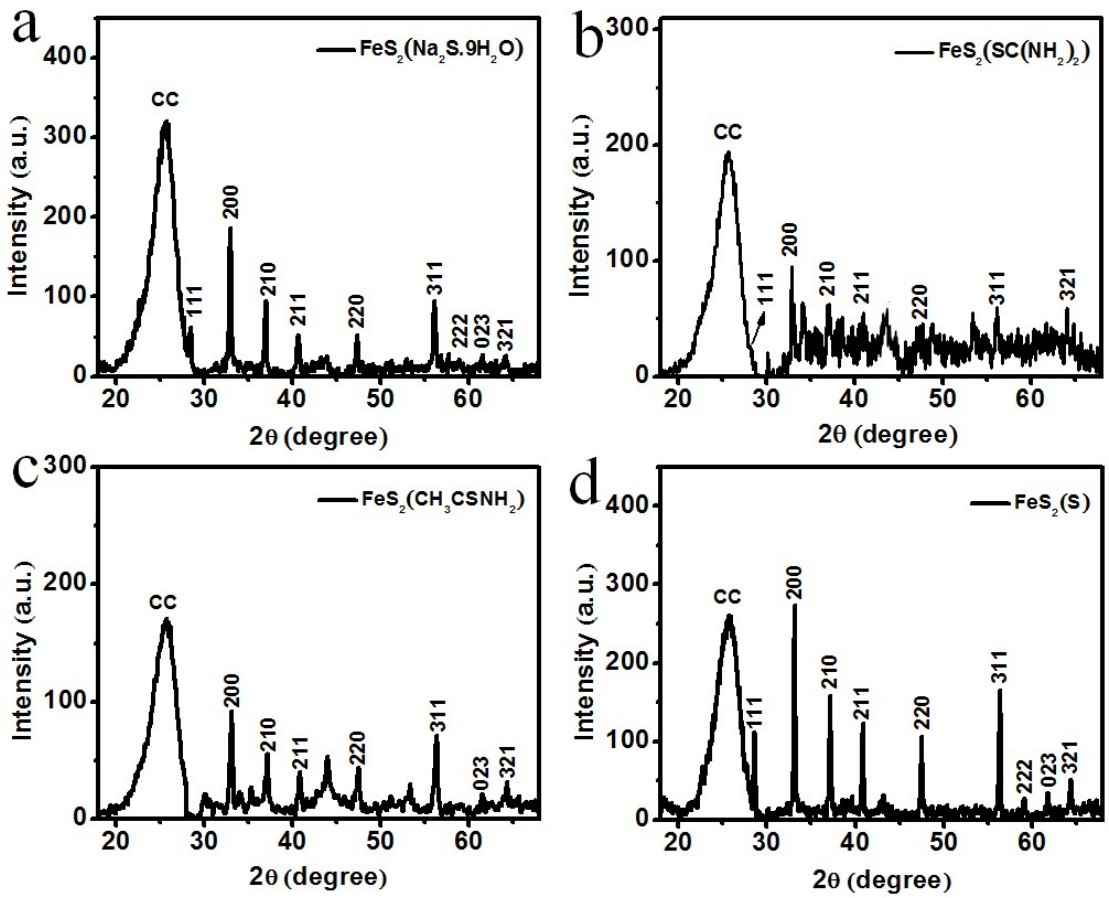

Fig. S1. (a-d) XRD pattern of $FeS_2(Na_2S{\cdot}9H_2O)$, $FeS_2(SC(NH_2)_2)$, $FeS_2(CH_3CSNH_2)$, and $FeS_2(S)$.

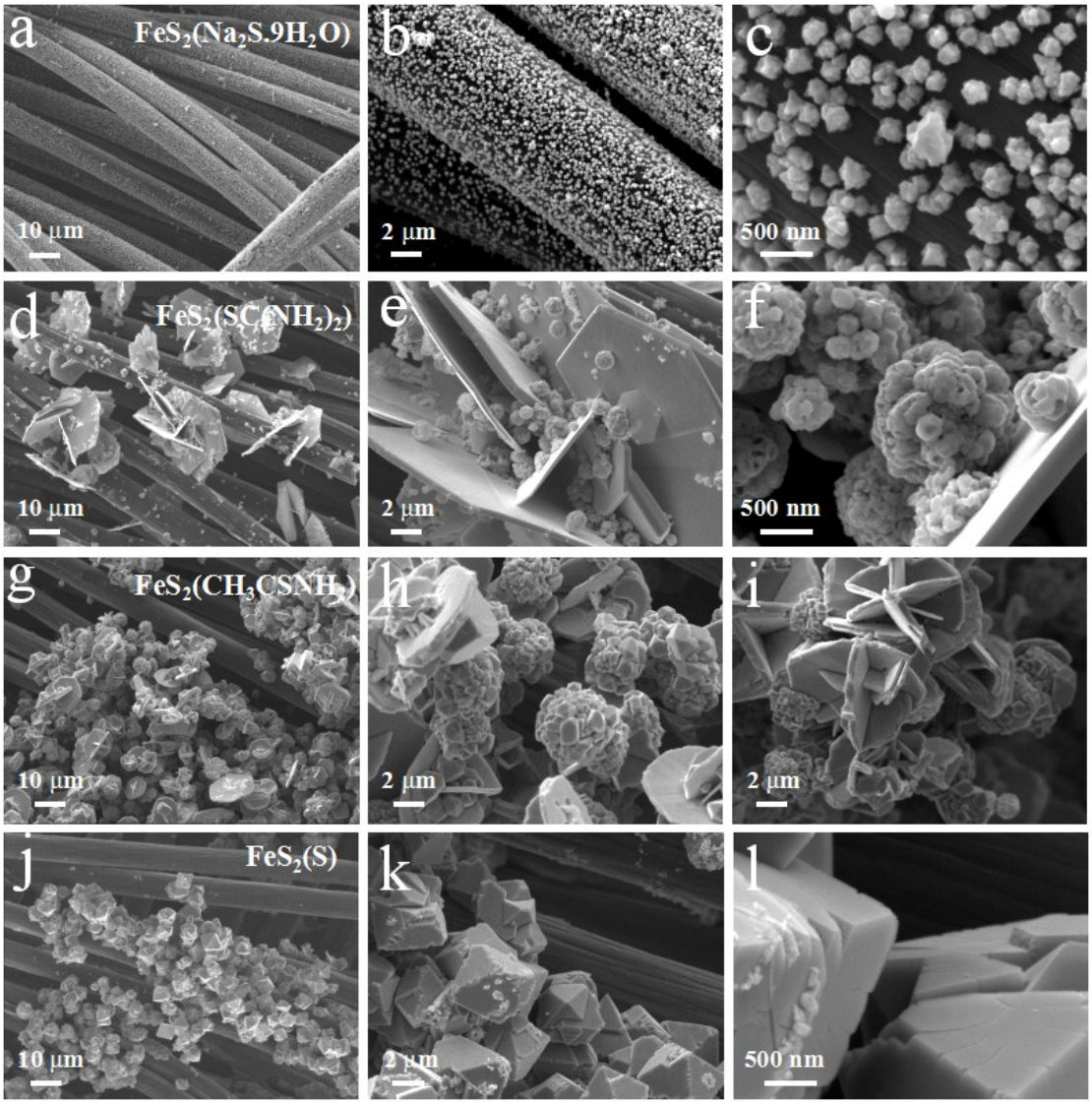

Fig. S2. (a-c) SEM images of $FeS_2(Na_2S{\cdot}9H_2O)$; (d-f) SEM images of $FeS_2(SC(NH_2)_2)$; (g-i) SEM images of $FeS_2(CH_3CSNH_2)$; (j-l) SEM images of $FeS_2(S)$.

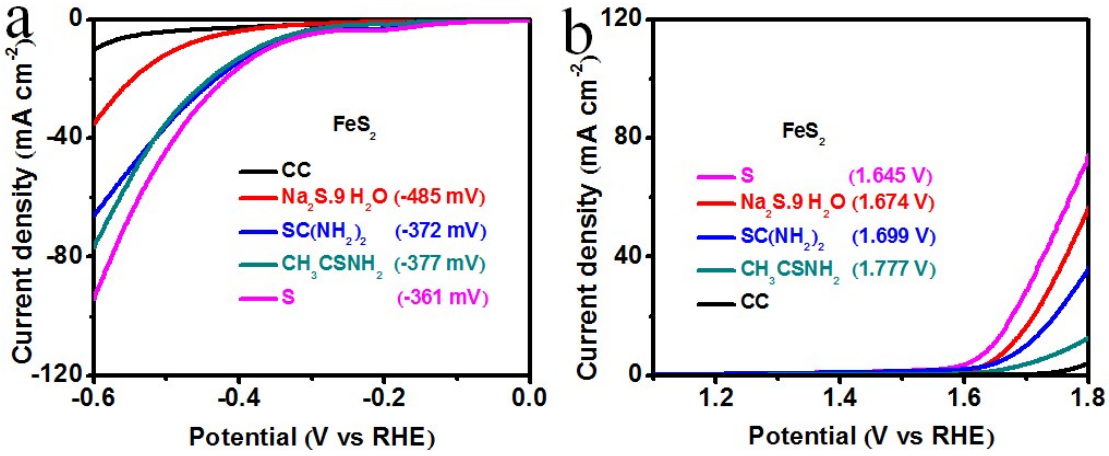

Fig. S3. (a) LSV curves of $FeS_2(Na_2S{\cdot}9H_2O)$, $FeS_2(SC(NH_2)_2)$, $FeS_2(CH_3CSNH_2)$, $FeS_2(S)$, and bare CC for HER; (b) LSV curves of $FeS_2(S)$, $FeS_2(Na_2S{\cdot}9H_2O)$, $FeS_2(SC(NH_2)_2)$, $FeS_2(CH_3CSNH_2)$, and bare CC for OER.

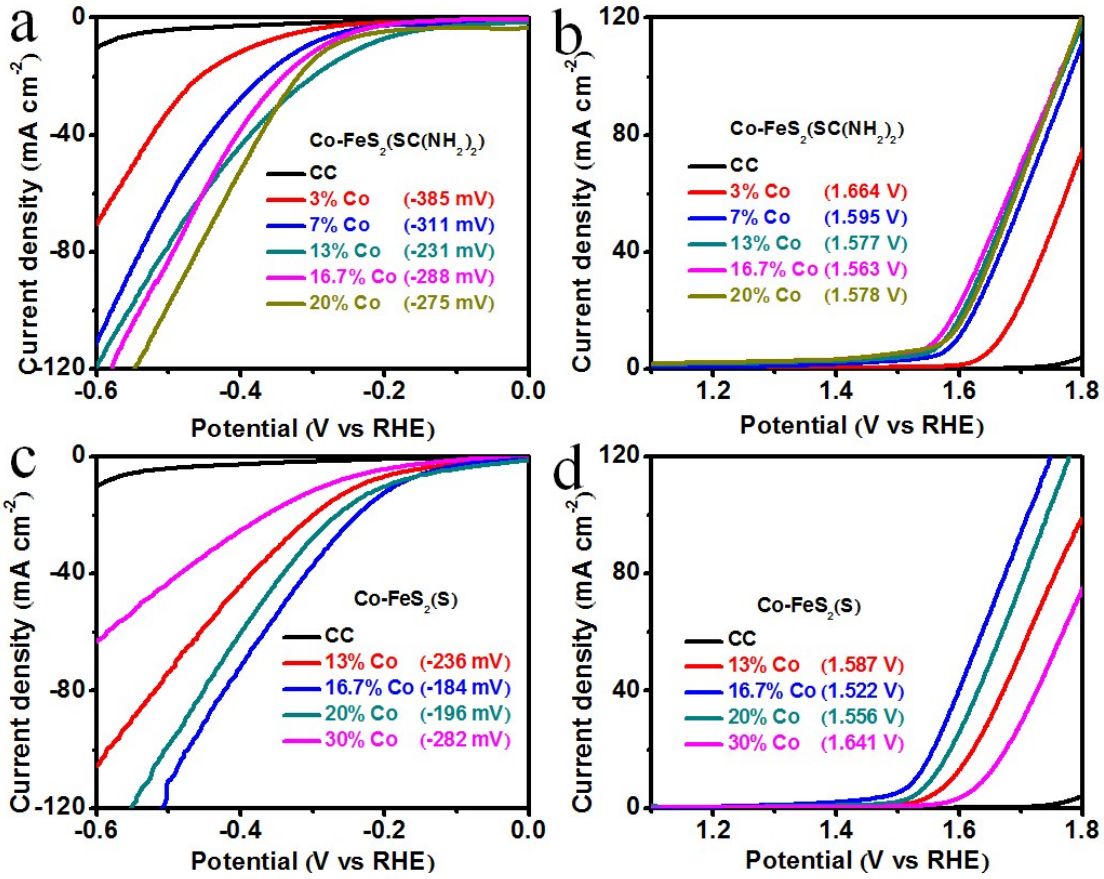

Fig. S4. (a) LSV curves of Co-$FeS_2(SC(NH_2)_2)$ with different cobalt doping ratios for HER; (b) LSV curves of Co-$FeS_2(SC(NH_2)_2)$ for OER; (c) LSV curves of Co-FeS_2(S) with different cobalt doping ratios for HER; (d) LSV curves of Co-FeS_2(S) for OER.

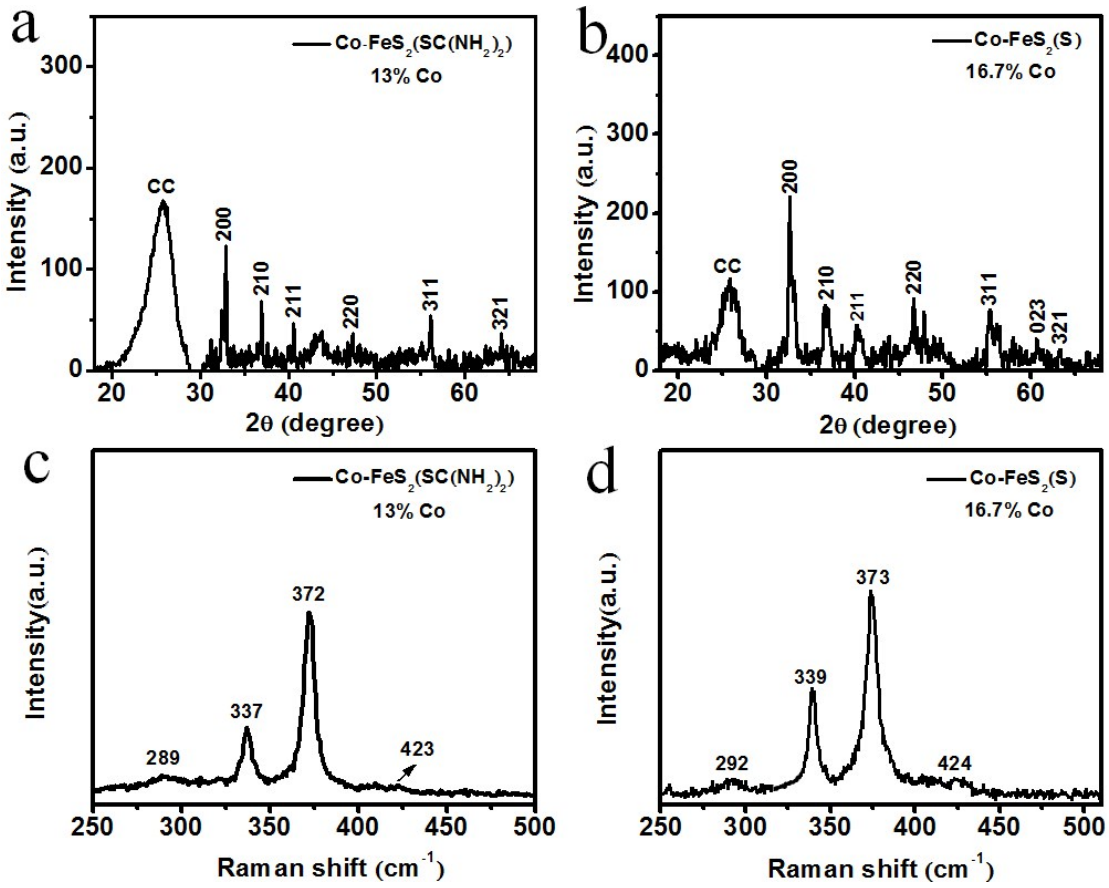

Fig. S5. (a) and (b) XRD pattern of the Co-$FeS_2(SC(NH_2)_2)$ and Co-FeS_2(S); (c), and (d) Raman spectra for Co-$FeS_2(SC(NH_2)_2)$ and Co-FeS_2(S).

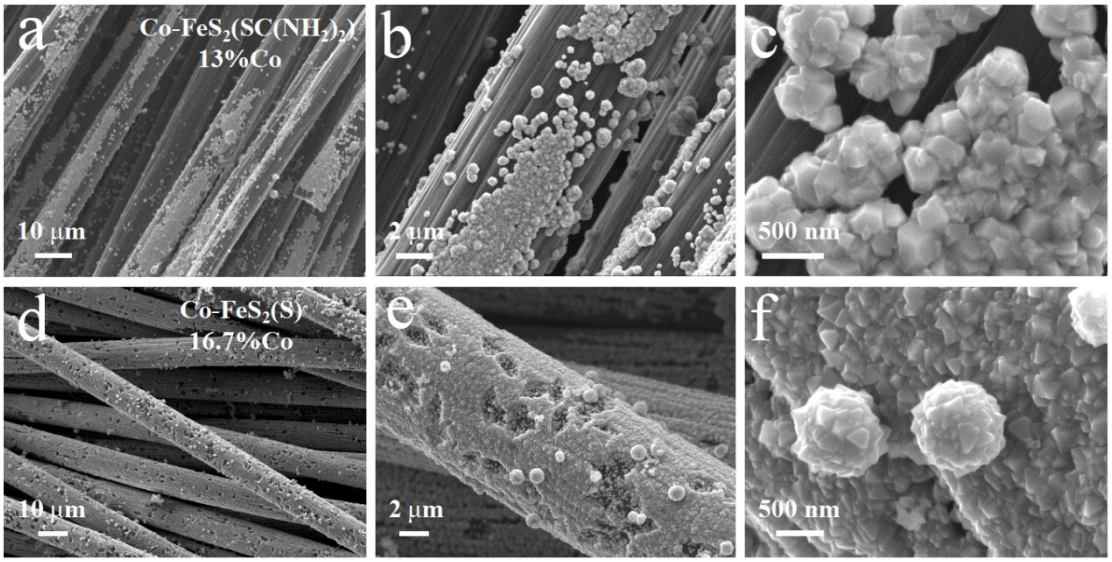

Fig. S6. (a-c) SEM images of Co-$FeS_2(SC(NH_2)_2)$; (d-f) SEM images of Co-FeS_2(S).

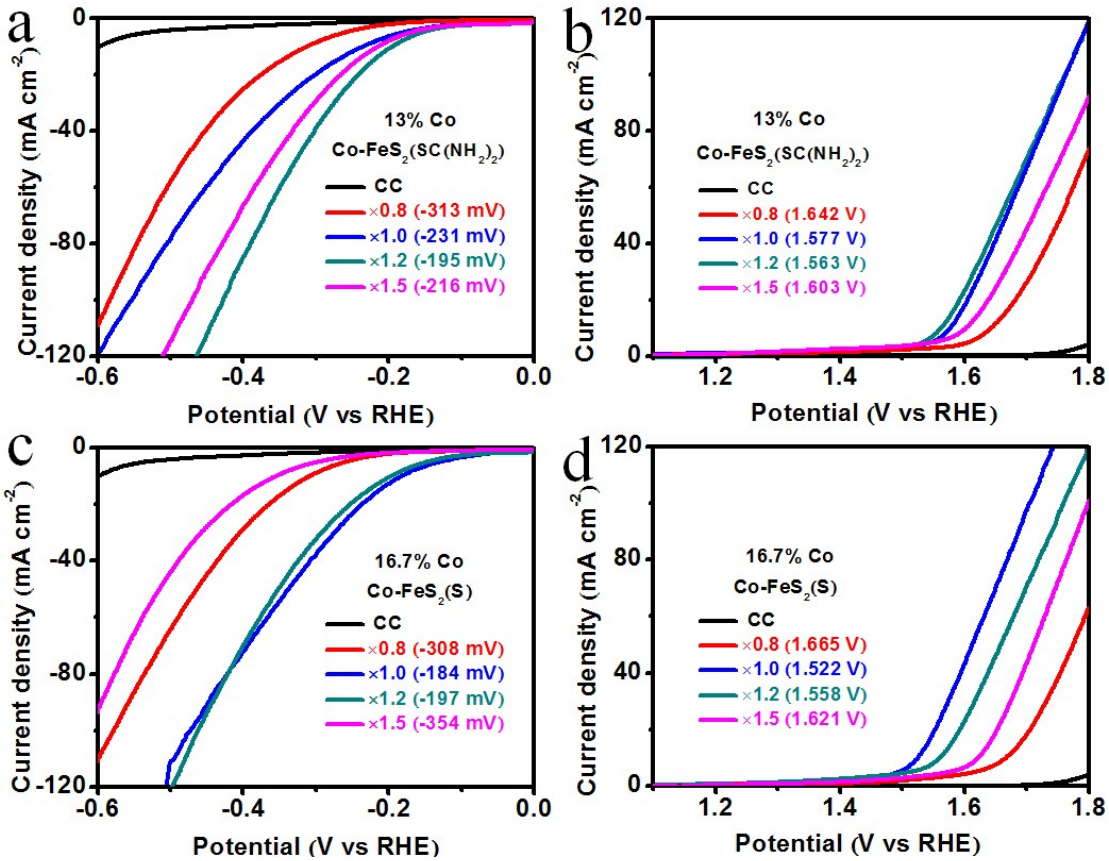

Fig. S7. (a) LSV curves of Co-FeS_2(S) for OER with different molar ratios; (b) LSV curves of Co-FeS_2(S) for OER; (c) LSV curves of Co-$FeS_2(SC(NH_2)_2)$ for OER with different molar ratios; (d) LSV curves of Co-$FeS_2(SC(NH_2)_2)$ for OER.

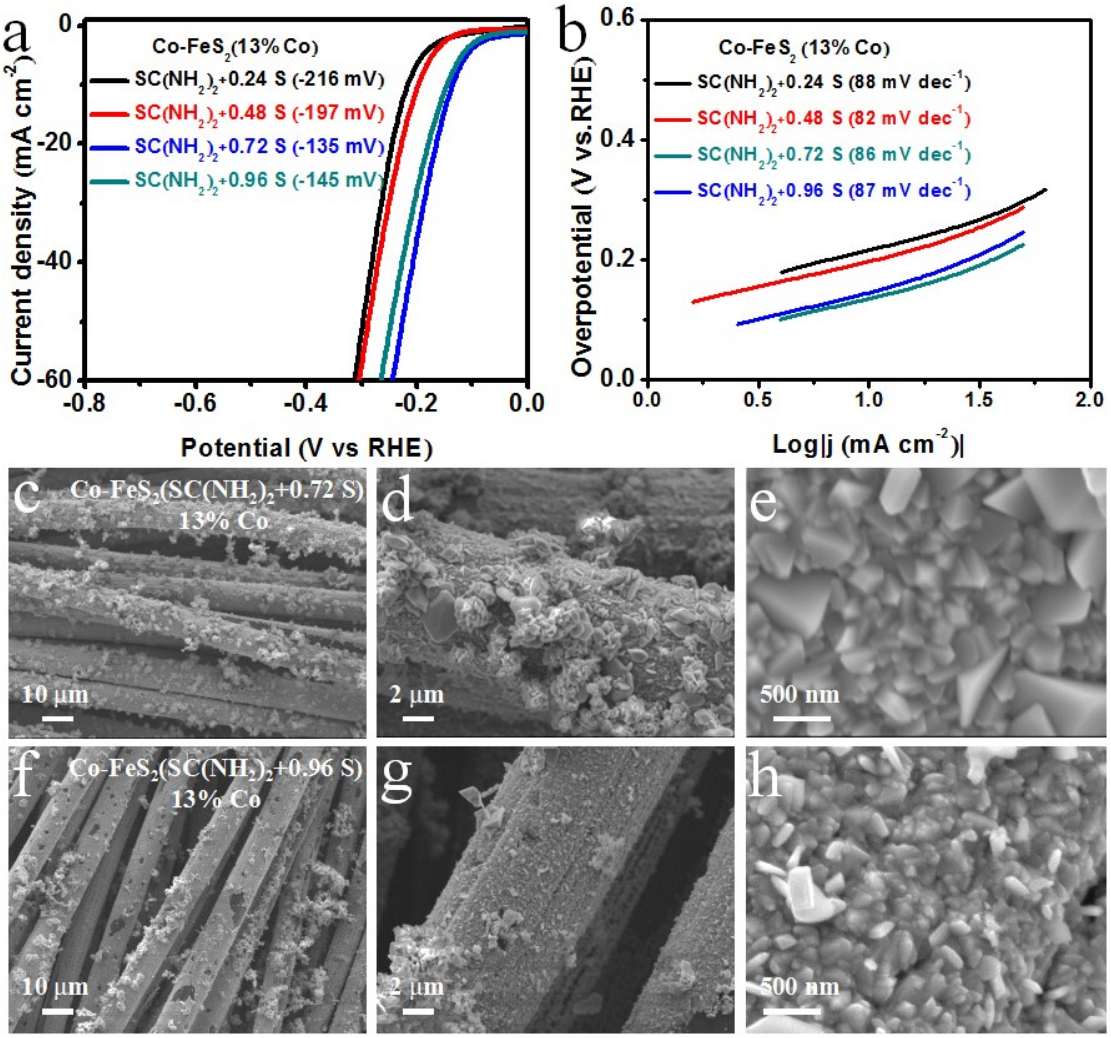

Fig. S8. (a) LSV curves of Co-FeS_2($SC(NH_2)_2$+xS x=0.24, 0.48, 0.72, 0.96) for HER with different molar ratios; (b) Corresponding tafel plots; (c-e) SEM images of Co-FeS_2($SC(NH_2)_2$+0.72 S); (f-h) SEM images of Co-FeS_2($SC(NH_2)_2$+0.96 S).

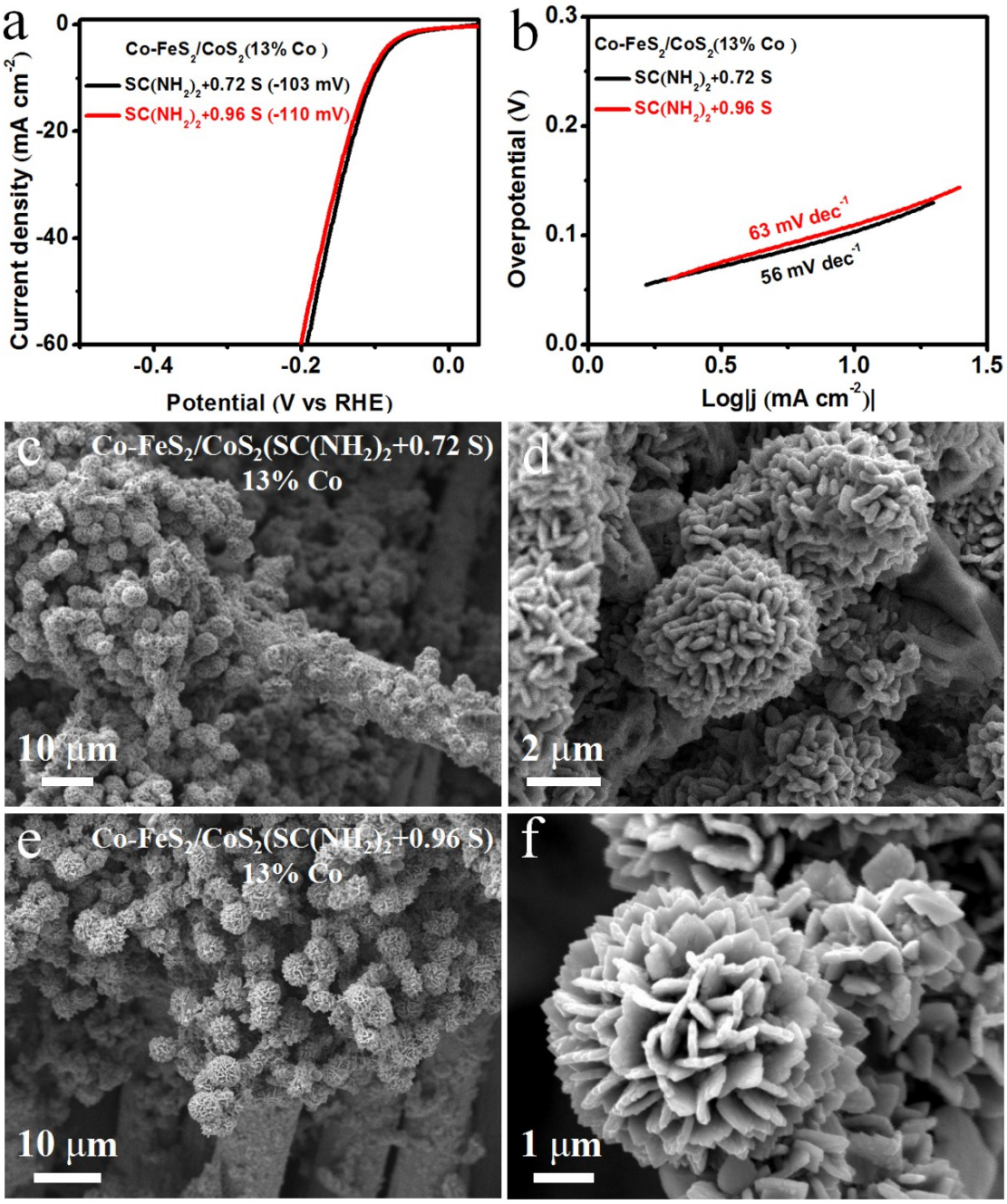

Fig. S9. (a) LSV curves of Co-FeS_2/CoS_2($SC(NH_2)_2$+0.72 S) and Co-FeS_2/CoS_2 ($SC(NH_2)_2$+0.96 S) after optimization for HER; (b) Corresponding tafel plots; (c), and (d) SEM images of optimized Co-FeS_2/CoS_2($SC(NH_2)_2$+0.72 S); (e), and (f) SEM images of optimized Co-FeS_2/CoS_2($SC(NH_2)_2$+0.96 S).

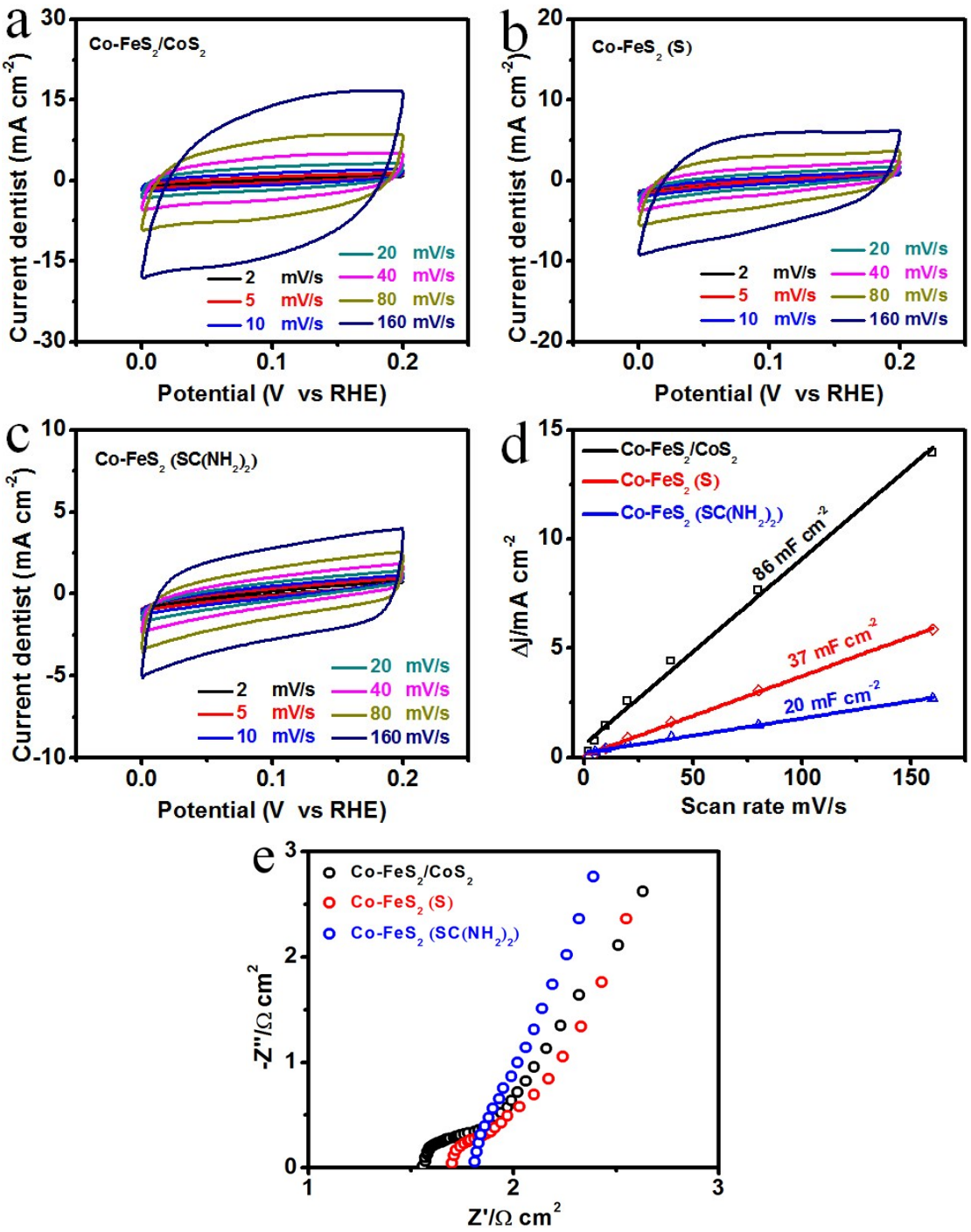

Fig. S10. (a-c) Cyclic voltammograms of Co-FeS_2/CoS_2, Co-FeS_2(S), and Co-FeS_2 ($SC(NH_2)_2$) were measured in the non-faradaic capacitance current range at scan rates of 2, 5, 10, 20, 40, 80, and 160 mV s^{-1}; (d) The capacitive currents at 0.1V as a function of scan rate for Co-FeS_2/CoS_2, Co-FeS_2(S), and Co-FeS_2 ($SC(NH_2)_2$); (e) EIS spectra of Co-FeS_2/CoS_2, Co-FeS_2(S), and Co-FeS_2 ($SC(NH_2)_2$).

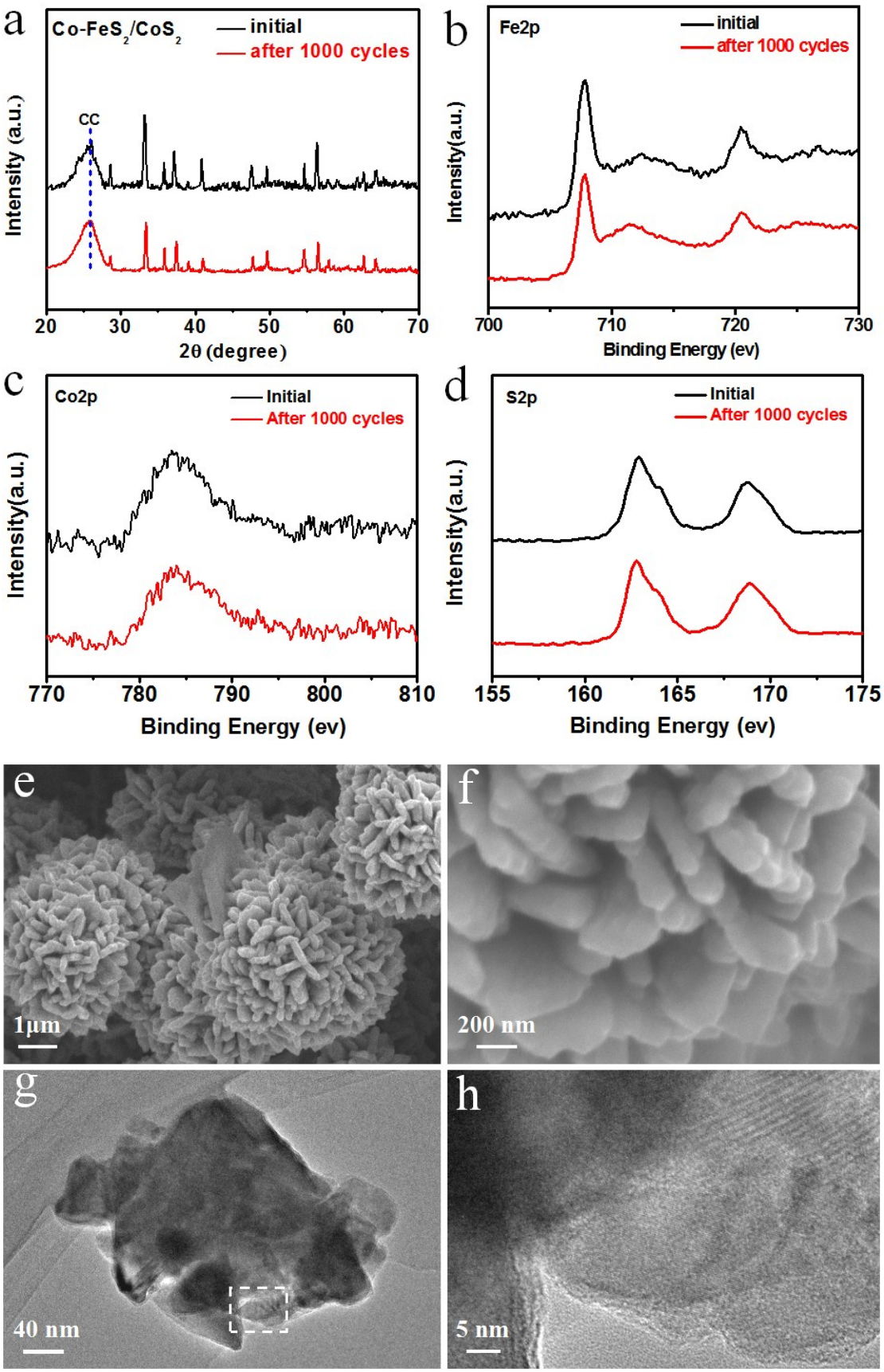

Fig. S11. (a) XRD patterns for Co-FeS_2/CoS_2; XPS spectra of the Co-FeS_2/CoS_2 from

(b) Fe2p, (c) Co2p, (d) S2p initial and after 1000 cycles; (e) and (f) SEM images of Co-FeS_2/CoS_2 after the 1000 cycles; (g) and (h) TEM images of Co-FeS_2/CoS_2 after the 1000 cycles.